ICES REPORT 13-25

August 2013

An Augmented-Lagrangian Method for the Phase-Field Approach for Pressurized Fractures

by

Mary F. Wheeler, Thomas Wick, Winnifried Wollner

The Institute for Computational Engineering and Sciences
The University of Texas at Austin
Austin, Texas 78712

Reference: Mary F. Wheeler, Thomas Wick, Winnifried Wollner, An Augmented-Lagrangian Method for the Phase-Field Approach for Pressurized Fractures , ICES REPORT 13-25, The Institute for Computational Engineering and Sciences, The University of Texas at Austin, August 2013.

An Augmented-Lagrangian Method for the Phase-Field Approach for Pressurized Fractures

M.F. Wheeler[a], T. Wick[a,*], W. Wollner[b]

[a] *The Institute for Computational Engineering and Sciences, The University of Texas at Austin, Austin, Texas 78712, USA*
[b] *Department of Mathematics, University of Hamburg 20146 Hamburg, Germany*

Abstract

In the modeling of pressurized fractures using phase-field approaches, the irreversibility of crack growth is enforced through an inequality constraint on the temporal derivative of the phase-field function. In comparison to the classical case in elasticity, the presence of the pressure requires the additional constraint and makes the problem much harder to analyze. After temporal discretization, this induces a minimization problem in each time step over a solution dependent admissible set. To avoid solving the resulting variational inequality corresponding to the first order necessary conditions; commonly a penalization approach is used to remove the inequality constraint. It is well-known that for large penalty parameters the algorithm suffers from numerical instabilities in the solution process. Consequently, to avoid such a drawback, we propose an augmented Lagrangian algorithm for the discrete in time and continuous in space phase-field problems. The final set of equations is solved in a decoupled fashion. The proposed method is substantiated with several benchmark and prototype tests in two and three dimensions.

Keywords: finite elements, phase-field, variational fracture, augmented Lagrangian, iterative solution
2010 MSC: 65N30, 65M60, 74F99

1. Introduction

Presently, crack propagation in elastic and porous media is one of the major research topics in energy and environmental engineering. Consequently, a huge variety of models and numerical techniques have been investigated so far.

*Corresponding author
Email addresses: mfw@ices.utexas.edu (M.F. Wheeler), twick@ices.utexas.edu (T. Wick), winnifried.wollner@uni-hamburg.de (W. Wollner)

Specifically, Griffith's model [1] for quasi-static fracture evolution has been successfully applied. Here, the crack propagates if the rate of elastic energy decrease per unit surface area of the increment step is equal to the quasi-static critical energy release rate G_c. The crack does not move if the elastic energy release rate is less than G_c. On the contrary, it is unstable if G_c exceeds the critical rate. Griffith found that G_c is related to the crack surface energy increase. The solution of crack representation and propagation requires special techniques for their numerical treatment. In recent years, different approaches have been proposed such as the extended finite element method by Moes et al. [2] based on the partition of unity method of Babuska and Belenk [3] in which the displacement field is enriched with discontinuities. In addition, fixed-mesh approaches such as phase-field techniques have gained increased interest by studies from Francfort and Marigo [4], Bourdin et al. [5, 6], Miehe et al. [7, 8], Borden et al. [9], Hofacker and Miehe [10]. Instead of modeling the discontinuities explicitly (like in the extended finite element method), the lower-dimensional crack surface is approximated by a phase-field function. This introduces a diffusive transition zone (brittle zone or mushy-zone are also common expressions depending on the discipline) between the broken and the unbroken material; see Figure 1.

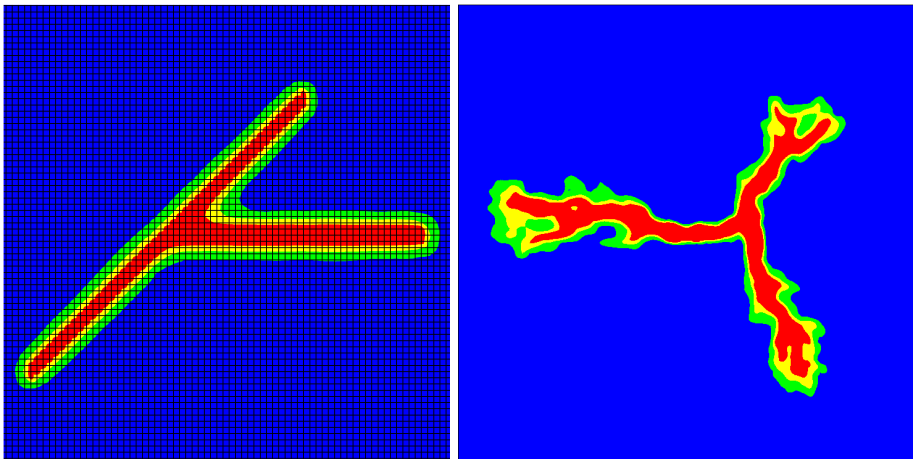

Figure 1: Explication of the fixed-grid finite element phase-field approach: A (lower-dimensional) crack is approximated with the help of a phase-field function as shown in the left figure. The phase-field is an indicator function with values 0 in the crack (here in red) and 1 in the unbroken zone (here in blue). The mushy-zone provides a smooth interpolation between 0 and 1 indicated in yellow and green. On the right side, the major advantages for the phase-field approach are shown: joining, branching and nonplanar crack growth in possibly heterogeneous media (figure taken from [11]).

The major advantages of using phase-field modeling for crack propagation are three-fold. First, it is a fixed-mesh approach in which remeshing is avoided. Second, the model is purely based on energy minimization and therefore, crack nucleation, propagation and the path are automatically determined (avoiding calculation of additional components such as stress intensity factors). Third,

multiple joining and branching of cracks do not require any additional techniques. Consequently, phase-field modeling allows simple handling of large and complex fracture networks. Quantities of interest such as the crack opening displacement (the aperture) can be recovered with the help of the phase-field function. From the application point of view, we are specifically interested in pressurized fractures and their propagation, which are of particular interest in dam constructions, subsurface modeling, blood flow with damaged tissue, and oil recovery processes. In recent years, several methods for pressurized fracture and crack propagation have been proposed. These include an implicit moving mesh algorithms of Lecampion and Detournay [12]; moving-mesh approach with local grid refinement by Schrefler et al. [13]; a special zero-thickness finite element approach by Carrier and Granet [14]; the partition of unity and extended finite element approaches by Irzal et al. [15]; and finally, boundary element approaches by Ganis et al. [16], Castonguay et al. [17]. To the best of our knowledge, the previously mentioned phase-field approach was first applied to pressurized cracks by Bourdin et al. [18], and a rigorous model investigation was first undertaken by Mikelić et al. [19, 11].

In this paper, we extend the previous studies [19, 11]. Namely, the penalization of the irreversibility condition for crack growth is modified. It is well-known from Lootsma [20], Murray [21] that simple penalization leads to numerical instabilities due to ill-conditioning of the constraint Hessian. Consequently, another (but computational costly) method is proposed by Mikelić et al. [11]. We circumvent these drawbacks in adapting a robust method from optimization: the augmented Lagrangian method dating back to Hestenes [22] and Powell [23] and proposed by Fortin and Glowinski [24], Glowinski and Tallec [25] for use in discretized differential equations. In particular, we consider the augmented Lagrangian in a function space setting similar to Ito and Kunisch [26, Chapter 4].

The numerical discretization is based on the incremental formulation [11]. In particular, a Galerkin finite element scheme is used for spatial discretization. The solution algorithm is based on a decoupling of the equations, which allows for easy extension to sophisticated solvers for each of the subproblems. This is in particular interesting for large-field 3d simulations. Since the augmented Lagrangian method is based on an iteration itself, we perform several subiterations until the change in displacements is sufficiently small. The nonlinear phase-field equation is solved with Newton's method whereas the elasticity problem is linear.

The paper is organized as follows: In Section 2, we recall the energy functionals defined on the continuous level. In Section 3, the augmented Lagrangian is derived with respect to the energy functional. Next, in Section 4, the corresponding Euler-Lagrange equations and their discretization are discussed. Moreover, our solution algorithm is described. The final Section 5 presents four different examples for pressurized cracks in two and three dimensions. We propose simple configurations that might allow comparisons with other methods for crack propagation and we provide a deeper understanding of the capabilities of our method by studying several numerical aspects.

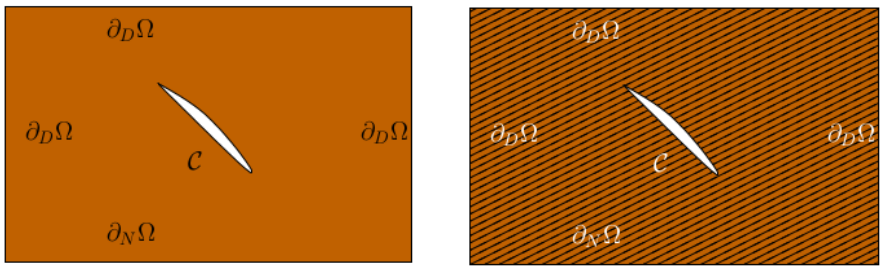

Figure 2: Prototype configurations of the setting. The difference between Bourdin's approach [18] (left) and our approach (right) is that he works in an elastic medium whereas we work in a poroelastic setting.

2. The Energy Functional

Let $\Omega \in \mathbb{R}^d$, $d = 2, 3$ be a given domain. We assume that the crack $\mathcal{C}$ is contained compactly in Ω, i.e., it does not reach the boundary. Let us denote by $(\cdot,\cdot)_A, \|\cdot\|_A$ the usual L^2-inner product and norm on A. If $A = \Omega$ we skip the subscript for better readability.

Following Griffith's criterion, we suppose that the crack propagation occurs when the elastic energy restitution rate reaches its critical value G_c. If τ is the traction force applied at the part of the boundary $\partial_N\Omega$, we then associate to the crack $\mathcal{C}$ the following total energy

$$\begin{aligned} E(u,\mathcal{C}) = \frac{1}{2}(\mathcal{G}e(u), e(u))_{\Omega\setminus\mathcal{C}} - (\tau, u)_{\partial_N\Omega} \\ - (\alpha-1)(p_B, \operatorname{div} u)_{\Omega\setminus\mathcal{C}} + (\nabla p_B, u)_{\Omega\setminus\mathcal{C}} + G_c\mathcal{H}^{d-1}(\mathcal{C}), \end{aligned} \tag{1}$$

where u denotes the vector-values displacement field, p_B is the poroelastic medium pressure, $\alpha \in [0,1]$ is the Biot coefficient, $\mathcal{H}^{d-1}$ is the $d-1$-dimensional Hausdorff measure, and $\mathcal{G}$ the rank-4 Gassman tensor. Later, we use the law

$$\mathcal{G}e(u) = \sigma(u) = 2\mu_s e(u) + \lambda_s \operatorname{tr} e(u) I,$$

where μ_s and λ_s denote the Lamé coefficients, $e(u) = \frac{1}{2}(\nabla u + \nabla u^T)$, and I the identity in d-dimensions.

This energy functional is then minimized with respect to the kinematically admissible displacements u and any crack set satisfying a crack growth condition. The computational modeling of this minimization problem should treat complex crack topologies and requires approximation of the crack location and of its length. This can be overcome by regularizing the sharp crack surface topology in the solid by diffusive crack zones described by a scalar auxiliary variable. This variable is a phase-field that interpolates between the unbroken and the broken states of the material. As previously stated above for the purely solid mechanics problem variational methods were introduced by Bourdin et al. [5, 6].

We introduce the time-dependent crack phase-field φ, defined on $\Omega \times (0,T)$. The regularized crack functional reads

$$\Gamma_\varepsilon(\varphi) = \frac{1}{2\varepsilon}\|(1-\varphi)\|^2 + \frac{\varepsilon}{2}\|\nabla\varphi\|^2 = \int_\Omega \gamma(\varphi, \nabla\varphi)\ dx, \tag{2}$$

where γ is the crack surface density per unit volume. This regularization of $\mathcal{H}^{d-1}(\mathcal{C})$, in the sense of the $\Gamma-$limit when $\varepsilon \to 0$, was used in [5, 6].

Our modeling part is based on the fact that the crack can only grow, which is represented by the irreversibility constraint:

$$\partial_t \varphi \leq 0. \tag{3}$$

In the following, we replace the energy (1) by a global constitutive dissipation functional for a rate independent fracture process [7, 18, 19]. We obtain then

$$\begin{aligned} E_\varepsilon(u,\varphi) = \frac{1}{2}\Big(\big((1-\kappa)\varphi^2+\kappa\big)\mathcal{G}e(u), e(u)\Big) - (\tau, u)_{\partial_N\Omega} \\ - (\alpha-1)(\varphi^2 p_B, \operatorname{div} u) + (\varphi^2\nabla p_B, u) \\ + G_c\bigg(\frac{1}{2\varepsilon}\|1-\varphi\|^2 + \frac{\varepsilon}{2}\|\nabla\varphi\|^2\bigg), \end{aligned} \tag{4}$$

where κ is a positive regularization parameter for elastic energy, with $\kappa \ll \varepsilon$. We remark that the meaning of the different terms in (4). The first term denotes the elastic bulk energy and the final term characterizes the surface energy of the crack. These two terms are already well-known from the pure elastic case. The middle line is novel and is a contribution from the pressure in the fracture.

In the following, we work in a quasi-static formulation and velocity changes are assumed to be negligible. Consequently, we replace the time derivative $\partial_t\varphi$ by a backward difference quotient

$$\partial_t\varphi \ \approx\ \partial_k\varphi = \frac{\varphi - \varphi^{n-1}}{k},$$

where $k > 0$ denotes the time step parameter and $\varphi := \varphi^n$ the present solution and φ^{n-1} the solution to the previous time step. Discretization in time at this stage leads to an incremental formulation. With this we have

$$\varphi \leq \varphi^{n-1}$$

which means that the crack should not shrink in each incremental step. Remember (see Figure 1) that the crack region is characterized by $\varphi = 0$ and the non-fractured zone by $\varphi = 1$.

3. The Augmented Lagrangian Method

The major novelty in this study is to impose the irreversibility constraint (3). To pose it in a minimization setting in function spaces, let us denote

$V := H_0^1(\Omega)$ and $W := H^1(\Omega)$. Then given a previous time step solution $(u^{n-1}, \varphi^{n-1}) \in V \times W$ we seek find $(u^n, \varphi^n) \in V \times W$ satisfying

$$\begin{aligned} &\min E_\epsilon(u^n, \varphi^n) \\ &\quad \text{s.t. } \varphi^n \in K(\varphi^{n-1}) := \{\varphi \,|\, 0 \le \varphi^n \le \varphi^{n-1} \le 1\}, \end{aligned} \tag{5}$$

or equivalently

$$\min E_\epsilon(u^n, \varphi^n) + I_{K(\varphi^{n-1})}(\varphi^n), \tag{6}$$

with the indicator function I_S of an arbitrary set S given by

$$I_S = \begin{cases} 0 & \text{on } S, \\ \infty & \text{otherwise.} \end{cases}$$

Since $K(\varphi^{n-1})$ is closed, convex, and non empty $I_{K(\varphi^{n-1})} \colon L^2(\Omega) \to \mathbb{R} \cup \{\pm\infty\}$ is proper, convex, and lower semi-continuous.

A rather simple penalization technique, to eliminate the extended real valued function $I_{K(\varphi^{n-1})}$, is used in [19], where the approximation

$$I_{K(\varphi^{n-1})} \approx \gamma \Big((\varphi - \varphi^{n-1}) \big)^+ \Big)^2,$$

for $\gamma \to \infty$ is considered. Here we denote by the superscript $+$ the positive part of a function, i.e.,

$$f^+ = \max(0, f).$$

However, it is well-known that this leads to numerical instabilities in the solution process. Another penalization of theoretical importance is employed in [11]. This one has however the drawback that it is very difficult to implement and rather expensive since second order derivatives need to be evaluated. Consequently, we aim for a simple but powerful strategy, which is provided by the augmented Lagrangian penalization. It is well-known in approaches as constraint optimization and in solving variational inequalities.

To avoid the non-differentiability of $I_{K(\varphi^{n-1})}$, while not increasing $\gamma \to \infty$, we introduce its Moreau-Yosida approximation, see, e.g., [26, Section 4.4]. To do so, let $\gamma \in \mathbb{R}_{>0}$, $\varphi, \lambda \in L^2(\Omega)$ be given. We define

$$M_\gamma(\varphi, \lambda) = \inf_{\psi \in L^2(\Omega)} \Big(I_{K(\varphi^{n-1})}(\varphi - \psi) + (\lambda, \psi) + \tfrac{\gamma}{2} \|\psi\|^2 \Big). \tag{7}$$

M_γ is, again, convex and Frechét differentiable with respect to φ, see, e.g., [26, Theorem 4.39]. In the present case, the unique minimizer φ_γ on the right of the

definition of $M_\gamma(\varphi,\lambda)$ in (7) is given by

$$\begin{aligned}
\varphi_\gamma &= \min\big(\varphi, \max\big(\varphi-\varphi^{n-1}, \tfrac{-1}{\gamma}\lambda\big)\big)\\
&= \min\big(\varphi, (\varphi-\varphi^{n-1}) + \big((\varphi^{n-1}-\varphi) - \tfrac{1}{\gamma}\lambda\big)^+\big)\\
&= \min\Big(\varphi, (\varphi-\varphi^{n-1}) + \tfrac{1}{\gamma}\lambda + \big((\varphi^{n-1}-\varphi) - \tfrac{1}{\gamma}\lambda\big)^+ - \tfrac{1}{\gamma}\lambda\Big)\\
&= \min\bigg(\varphi, \frac{1}{\gamma}\Big(\big(\lambda+\gamma(\varphi-\varphi^{n-1})\big)^+ - \lambda\Big)\bigg)\\
&= \frac{1}{\gamma}\min\Big(\gamma\varphi, \big(\lambda+\gamma(\varphi-\varphi^{n-1})\big)^+ - \lambda\Big)\\
&= \frac{1}{\gamma}\Big(\min\Big(\lambda+\gamma\varphi, \big(\lambda+\gamma(\varphi-\varphi^{n-1})\big)^+\Big) - \lambda\Big).
\end{aligned}$$

Hence

$$\begin{aligned}
M_\gamma(\varphi,\lambda) &= I_{K(\varphi^{n-1})}(\varphi-\varphi_\gamma) + (\lambda,\varphi_\gamma) + \tfrac{\gamma}{2}\|\varphi_\gamma\|^2\\
&= (\lambda,\varphi_\gamma) + \tfrac{\gamma}{2}\|\varphi_\gamma\|^2\\
&= \Big(\lambda + \tfrac{1}{2}\Big(\min\Big(\lambda+\gamma\varphi, \big(\lambda+\gamma(\varphi-\varphi^{n-1})\big)^+\Big) - \lambda\Big), \varphi_\gamma\Big)\\
&= \frac{1}{2\gamma}\Big(\lambda + \min\Big(\lambda+\gamma\varphi, \big(\lambda+\gamma(\varphi-\varphi^{n-1})\big)^+\Big), \gamma\varphi_\gamma\Big)\\
&= \frac{1}{2\gamma}\bigg\|\min\Big(\lambda+\gamma\varphi, \big(\lambda+\gamma(\varphi-\varphi^{n-1})\big)^+\Big)\bigg\|^2 - \frac{1}{2\gamma}\|\lambda\|^2.
\end{aligned}$$

Noting that if $\big(\lambda+\gamma(\varphi-\varphi^{n-1})\big)^+ \neq 0$ then it holds

$$\big(\lambda+\gamma(\varphi-\varphi^{n-1})\big)^+ = \lambda+\gamma(\varphi-\varphi^{n-1}) \leq \lambda+\gamma\varphi$$

and thus it is

$$\min\Big(\lambda+\gamma\varphi, \big(\lambda+\gamma(\varphi-\varphi^{n-1})\big)^+\Big) = \big(\lambda+\gamma(\varphi-\varphi^{n-1})\big)^+.$$

Furthermore, it is

$$\lambda+\gamma\varphi \geq \lambda+\gamma(\varphi-\varphi^{n-1}) = \big(\lambda+\gamma(\varphi-\varphi^{n-1})\big)^+ \geq 0$$

and hence $\min(0,\lambda+\gamma\varphi) = 0$. In the other case, i.e., $\big(\lambda+\gamma(\varphi-\varphi^{n-1})\big)^+ = 0$ it holds

$$\min\Big(\lambda+\gamma\varphi, \big(\lambda+\gamma(\varphi-\varphi^{n-1})\big)^+\Big) = \min(0,\lambda+\gamma\varphi).$$

We conclude that we can rewrite $M_\gamma(\varphi,\lambda)$ as

$$\begin{aligned}
M_\gamma(\varphi,\lambda) &= \frac{1}{2\gamma}\Big\|\min(0,\lambda+\gamma\varphi) + \big(\lambda+\gamma(\varphi-\varphi^{n-1})\big)^+\Big\|^2 - \frac{1}{2\gamma}\|\lambda\|^2\\
&= \frac{1}{2\gamma}\Big\|\min(0,\lambda+\gamma\varphi)\Big\|^2 + \frac{1}{2\gamma}\Big\|\big(\lambda+\gamma(\varphi-\varphi^{n-1})\big)^+\Big\|^2 - \frac{1}{2\gamma}\|\lambda\|^2.
\end{aligned}$$

Its Frechét derivative with respect to φ is given by

$$M'_\gamma(\varphi,\lambda) = \min(0,\lambda+\gamma\varphi) + \big(\lambda+\gamma(\varphi-\varphi^{n-1})\big)^+.$$

Using these calculations, we introduce the augmented Lagrangian

$$L_\gamma(u,\varphi,\lambda) = E_\epsilon(u,\varphi) + M_\gamma(\varphi,\lambda),$$

and the corresponding method reads as follows:

Algorithm 1 Augmented Lagrangian Algorithm for the Solution of (5)

Choose $\lambda_0 \in L^2(\Omega)$, $\gamma > 0$, and let $k = 0$.
repeat
Find (u_{k+1}, φ_{k+1}) solving

$$\min_{u,\varphi} L_\gamma(u,\varphi,\lambda_k)$$

or equivalently

$$\min_{u,\varphi} E_\epsilon(u,\varphi) + \frac{1}{2\gamma}\big\|\min(0,\lambda+\gamma\varphi)\big\|^2 + \frac{1}{2\gamma}\big\|\big(\lambda_k+\gamma(\varphi-\varphi^{n-1})\big)^+\big\|^2.$$

Update

$$\lambda_{k+1} = M'_\gamma(\varphi_{k+1},\lambda_k)$$

$k \leftarrow k+1$
until Stopping criterion (8) is satisfied
$(u^n,\varphi^n) = (u_k,\varphi_k)$

Remark 3.1. In our calculations, a clever choice for the initial guess λ_0 is given by λ^{n-1} from the previous time step.

Applying [26, Theorem 4.45], for (u^n,φ^n) solving (5) it holds necessarily that there is some λ^n such that

$$\lambda^n = M'_\gamma(\varphi^n,\lambda^n), \quad (u^n,\varphi^n) = \operatorname{argmin} E_\epsilon(u,\varphi) + M_\gamma(\varphi,\lambda^n).$$

Hence a reasonable stopping criterion for Algorithm 1 is given by

$$\max(\|u_{k-1}-u_k\|, \|\lambda_{k-1}-\lambda_k\|) \le \mathrm{TOL} \tag{8}$$

for some given tolerance $\mathrm{TOL} > 0$.

4. Equations and Finite Element Implementation

In this section, we derive from the energy functional (6) the corresponding Euler-Lagrange equations in variational form. These equations are the basis of our Galerkin finite element discretization. Finally, we describe our decoupled solution algorithm.

4.1. The Euler-Lagrange equations

In order to apply a Galerkin finite element method, we need to derive the Euler-Lagrange equations to the energy functional

$$\min_{u,\varphi} E_\epsilon(u,\varphi) + \frac{1}{2\gamma}\big\|\big(\lambda_k + \gamma(\varphi - \varphi^{n-1})\big)^+\big\|^2.$$

Differentiating with respect to u and φ, we obtain:

$$\begin{aligned}\Big(\big((1-\kappa)\varphi^2+\kappa\big)\,\mathcal{G}e(u), e(w)\Big) - (\tau, w)_{\partial_N\Omega} \\ - (\alpha-1)(\varphi^2 p_B, \operatorname{div} w) + (\varphi^2\nabla p_B, w) = 0 \quad \forall w \in V,\end{aligned} \tag{9}$$

as well as

$$\begin{aligned}(1-\kappa)(\varphi\,\mathcal{G}e(u) : e(u), \psi) - 2(\alpha-1)(\varphi\, p_B \operatorname{div} u, \psi) + 2\,(\varphi\nabla p_B\, u, \psi) \\ + G_c\Big(-\frac{1}{\varepsilon}(1-\varphi,\psi) + \varepsilon(\nabla\varphi, \nabla\psi)\Big) \\ + \Big((\lambda + \gamma(\varphi - \varphi^{n-1}))^+, \psi\Big) = 0 \quad \forall\,\psi \in W.\end{aligned} \tag{10}$$

In order to solve both problems, we formulate a bilinear form for the linear elasticity part and a semi-linear form for the nonlinear phase-field as follows:

$$\begin{aligned}A_1(u,w) = \Big(\big((1-\kappa)\varphi^2+\kappa\big)\,\mathcal{G}e(u), e(w)\Big) - (\tau, w)_{\partial_N\Omega} \\ - (\alpha-1)(\varphi^2 p_B, \operatorname{div} w) + (\varphi^2\nabla p_B, w) = 0 \quad \forall w \in V,\end{aligned} \tag{11}$$

and

$$\begin{aligned}A_2(\varphi)(\psi) = (1-\kappa)(\varphi\,\mathcal{G}e(u) : e(u), \psi) \\ - 2(\alpha-1)(\varphi\, p_B \operatorname{div} u, \psi) + 2\,(\varphi\nabla p_B\, u, \psi) \\ + G_c\Big(-\frac{1}{\varepsilon}(1-\varphi,\psi) + \varepsilon(\nabla\varphi, \nabla\psi)\Big) \\ + \Big((\lambda + \gamma(\varphi - \varphi^{n-1}))^+, \psi\Big) = 0 \quad \forall\,\psi \in W.\end{aligned} \tag{12}$$

4.2. Galerkin finite element discretization

The computational domain is subdivided into quadrilateral or hexahedral element domains. Both subproblems are discretized using H^1-conforming bilinear elements, i.e., the ansatz and test space uses Q_1^c-finite elements. Consequently, the discrete spaces have the property $V_h \subset V$ and $W_h \subset W$. The elasticity problem is linear and can be treated with an appropriate solver. Thus, for any given $\varphi^h \in W_h$ we can find $u^h \in V_h$ solving

$$A_1(u^h, w) = 0 \quad \forall\, w \in V_h.$$

Vice versa, for any given $u^h \in V_h$ we can solve the nonlinear problem of finding φ^h solving (12) with Newton's method. For the iteration steps $m = 0, 1, 2, \ldots$, the Newton update is given by finding $\delta\varphi^h \in W_h$ solving:

$$\begin{aligned}A_2'(\varphi^{h,m})(\delta\varphi^h, \psi) = -A_2(\varphi^{h,m})(\psi) \quad \forall\psi \in W_h, \\ \varphi^{h,m+1} = \varphi^{h,m} + \omega\delta\varphi^h,\end{aligned} \tag{13}$$

with a line search parameter $\omega \in (0,1]$. Here, we need the Jacobian of $A_2(\varphi)(\psi)$ applied to a direction $\delta\varphi$:

$$\begin{aligned} A_2'(\varphi)(\delta\varphi,\psi) = (1-\kappa)\big(\delta\varphi \mathcal{G} e(u) : e(u), \psi\big) \\ - 2\,(\alpha-1)(\delta\varphi\; p_B \text{ div } u, \psi) + 2\,(\delta\varphi \nabla p_B\; w, \psi) \\ + G_c\Big(-\frac{1}{\varepsilon}(\delta\varphi,\psi) + \varepsilon(\nabla\delta\varphi, \nabla\psi)\Big) \\ + \gamma\,(\delta\varphi,\psi)_{\mathcal{A}(\varphi)} \end{aligned} \tag{14}$$

where

$$\mathcal{A}(\varphi) = \{x \in (0,L)^3 \mid \lambda + \gamma(\varphi - \varphi^{n-1}) > 0\}.$$

Summarizing, we deal with:

Problem 4.1 (Variational FE formulation for linear elasticity)**.** Find $u^h \in V_h$ such that

$$A_1(u^h, w) = 0, \quad \forall w \in V_h,$$

and

Problem 4.2 (Variational FE formulation for phase-field)**.** Find $\varphi^h \in W_h$ such that

$$A_2'(\varphi^{h,m})(\delta\varphi^h,\psi) = -A_2(\varphi^{h,m})(\psi), \quad \varphi^{h,m+1} = \varphi^{h,m} + \omega\delta\varphi^h, \tag{15}$$

for all $\delta\varphi^h \in W_h$ and where A_2 and A_2' are given by (12) and (14).

4.3. The solution algorithm

Following [11], we use the quasi-static splitting approach as solution algorithm. Here, both systems are solved subsequently in an iterative way. This allows for easy extension for the usage of specific solvers for each of the subproblems. Our strategy is as follows: at time step t^n, for the given iteration φ^{l-1}, we solve first for u^l and then for the new φ^l with given u^l. Thus,

Problem 4.3 (Iteration of the decoupled problem)**.** Let $\varphi^{h,l-1}$ be given from the previous iteration step. Find $u^{h,l} \in V_h$ such that

$$A_1(u^{h,l}, w) = 0, \quad \forall w \in V_h.$$

Take $u^{h,l}$ and solve for $\varphi^{h,l}$:

$$A_2'(\varphi^{h,m,l})(\delta\varphi^h,\psi) = -A_2(\varphi^{h,m,l})(\psi), \quad \varphi^{h,m+1,l} = \varphi^{h,m,l} + \omega\delta\varphi^h, \tag{16}$$

for all $\delta\varphi^h \in W_h$ and where A_2 and A_2' are given by (12) and (14). The iteration is stopped when

$$\max(\|u_{l-1} - u_l\|, \|\varphi_{l-1} - \varphi_l\|) \le \text{TOL}_2 \tag{17}$$

for some positive tolerance TOL_2.

For the sake of simplicity, we use direct solvers to solve the linear subproblems. However, the implementation of an iterative solver is straight forward.

The solution process is outlined in Algorithm 2.

Algorithm 2 Solution algorithm

For each time t^n
repeat
  Solve augmented Lagrangian loop
  repeat
    Solve two-field problem iteratively, namely
      Solve linear elasticity in Problem 4.1
      Solve the nonlinear phase-field in Problem 4.2.
  until Stopping criterion (17) for two-field iteration is satisfied
  Update

$$\lambda_{k+1} = (\lambda_k + \gamma(\varphi_{k+1} - \varphi^{n-1}))^+$$

until Stopping criterion (8) for augmented Lagrangian is satisfied
Set: $(u^n, \varphi^n) := (u_k, \varphi_k)$.
Increment $t^n \to t^{n+1}$.

5. Numerical Tests

We perform four numerical tests to investigate the augmented Lagrangian method. First, we compute Sneddon's 2d benchmark problem [27] (Chapter 2.4) with a constant pressure, which has been used in the literature for code validation [18, 19, 11]. In the second example, we consider a propagating crack, which is driven by an increasing pressure [11]. As third test case, two cracks are joining due to an increasing pressure. In fact, this example shows one of the advantages of the phase-field approach compared to other methods. In the final example, we compute Sneddon's 3d constant-pressure penny-shape crack [27] (Chapter 3.3). It is well-known that the phase-field approach needs fine meshes to work with sufficient accuracy. Thus, the aim of the study is to validate the proposed model by computing solutions on a hierarchy of locally refined meshes in which a priori knowledge of crack propagation is taken into account. However, a simple automated refinement technique would be to use the mushy-zone of the phase-field function to mark cells for refinement for the next time step. In fact, such an approach for mesh refinement using an initial-point-set function (which has the same purpose as a phase-field function) is used in [28]. To the best of our knowledge, detailed numerical verification for pressurized cracks using a phase-field approach has not yet been performed for the test cases 5.2, 5.3, 5.4. All examples are computed with the multiphysics template [29], based on the finite element software `deal.II` [30].

5.1. Sneddon's 2D benchmark with constant pressure

The first example is motivated by Bourdin et al. [18] and is based on the theoretical calculations of Sneddon and Lowengrub [27], Sneddon [31]. Specifically, we consider a 2D problem where a (constant) pressure p_B is used to drive the deformation and crack propagation. We assume a dimensionless form of the equations. The configuration is displayed in Figure 5. Therefore, we deal with

the following geometric data: $\Omega = (0,4)^2$ and a (prescribed) initial crack with length $l_0 = 0.4$ on $\Omega_C = (1.8, 2.2) \times (2-h, 2-h) \subset \Omega$. As boundary conditions we set the displacements zero on $\partial\Omega$. The initial penalization is given by $\gamma = 10^4$. The tolerance for the augmented Lagrangian method is $\mathrm{TOL} = 10^{-4}$. We use a very loosely-coupled scheme in which we solve only once per subproblem and then proceed to the next time step. The time step loop is run until the tolerance is $\mathrm{TOL} = 10^{-5}$ is reached, i.e., $\|u^{n-1} - u^n\| \leq 10^{-5}$.

The Biot coefficient is $\alpha = 0$. The fracture toughness is chosen as $G_c = 1.0$. The mechanical parameters are Young's modulus and Poisson's ration $E = 1.0$ and $\nu_s = 0.2$. The relationship to the Lamé coefficients μ_s and λ_s is given by:

$$\mu_s = \frac{E}{2(1+\nu_s)}, \qquad \lambda_s = \frac{\nu_s E_s}{(1+\nu_s)(1-2\nu_s)}.$$

The injected pressure is $p_B = 10^{-3}$. Several parameters and geometry-related issues depend on the spatial mesh size parameter h. Namely, for the regularization parameters we choose the relations $\kappa = h, \varepsilon = 2h$. In addition, the initial (lower-dimensional) crack-line is extended by h in normal direction to approximate it as a volume as displayed in Figure 3. Finally, the evaluation points of the normal displacements are placed depending on h as well, shown in Figure 3, too.

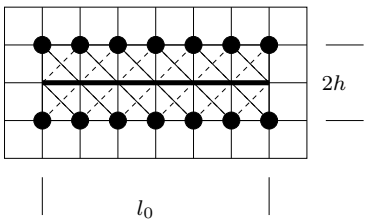

Figure 3: Zoom-in to the center of the domain Ω. The lower-dimensional crack with length $l_0 = 0.4$ (here a line in fat black) is approximated as a volume by extending it with mesh size h in normal up- and down-directions. The evaluation points for the normal displacements (to compute the COD) using Formula (18) are displayed as dark circles. The volume extension of the crack and the evaluation points depend therefore both on the choice of h.

Specifically, to compute the width w, we have two different formulas:

- The jump of the normal displacements:

$$w = COD = [u(x,y) \cdot n(x,y)], \tag{18}$$

  with evaluation at the points as displayed in Figure 3.

- Integration in normal direction, such that

$$w = COD = \int_0^4 u(x_0,y) \cdot \nabla\varphi(x_0,y)\, dy, \tag{19}$$

  where φ is as before our phase-field function and x_0 the x-coordinate of the integration line.

The goals of our studies are summarized as follows:

- Measuring the crack opening displacement COD for different h and comparison to Sneddon's analytical results [27];
- Comparison of both COD evaluation formulas (18) and (19);
- Comparison of the number of augmented Lagrangian iterations for each time step with respect to different h.

Our results might also be compared to [27, 18, 19, 11]. The crack pattern and the corresponding mesh are displayed in Figure 5. In Figure 4, the crack opening displacement is shown. The solution on the finest meshes fits well with the analytical solution provided by Sneddon. Moreover, we observe that both evaluation formulas gives the same limit for decreasing h. As seen in Table 1, for the chosen tolerance 10^{-5} for the time step loop, we have a very good approximation after only one time step. This is in agreement with our expectations because the setting of this test is fully stationary. In all tests the time step tolerance is already reached in the second iteration. We also notice that in these two-dimensional test cases, good agreement of the functional values is already achieved on relative coarse meshes.

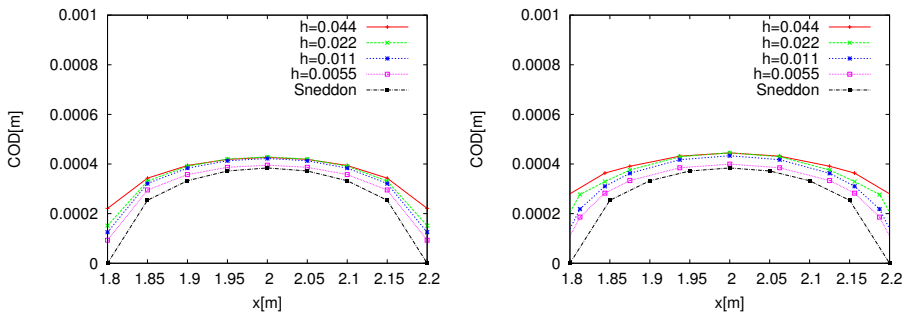

Figure 4: Example 1: COD for different h. In the plot, we have $h := h_{\min}$. Sneddon's black line corresponds to his analytical solution. On the left, the COD is computed with formula (18) and on the right with formula (19). Both formulas show good agreement in computing the COD.

Table 1: Comparison of λ-iterations for each time step with respect to h.

Timestep	$h_{\min}$	λ-iter
0	0.044	13
1	0.044	7
0	0.022	12
1	0.022	10
0	0.011	17
1	0.011	12
0	0.0055	22
1	0.0055	15

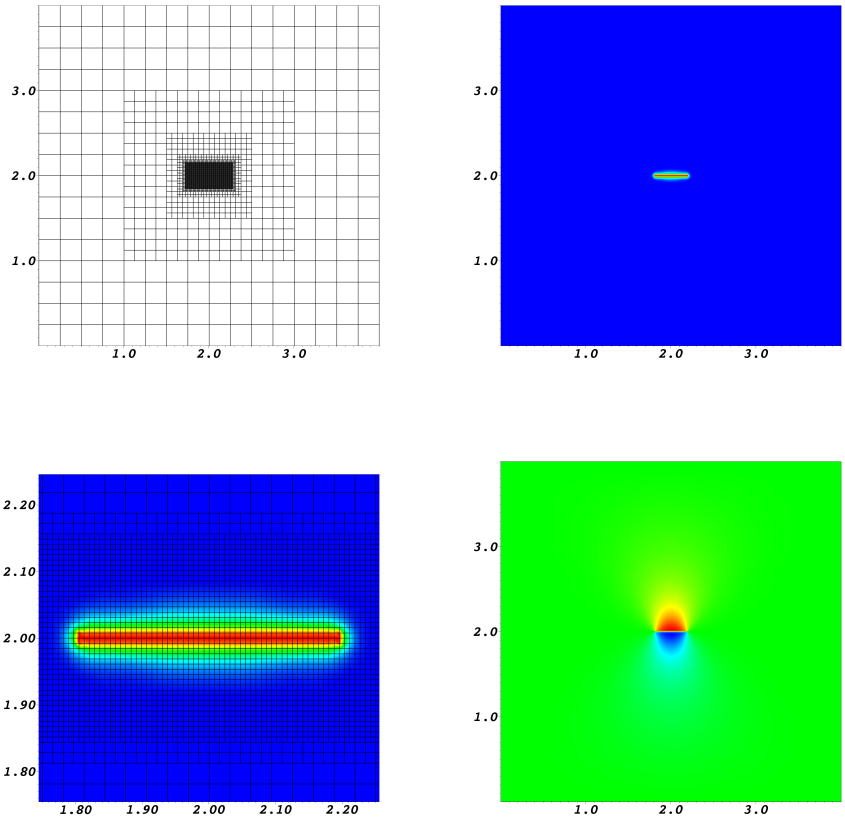

Figure 5: Example 1: Mesh and geometry, location of crack, zoom-in of the mesh with the crack pattern, and finally, normal displacements (required to compute the COD of the crack) are displayed from top left to bottom right. The green part in the third subfigure shows the thickness ε of the mushy-zone in the phase-field variable.

5.2. Increasing pressure leading to crack propagation

We keep the geometry, all parameters, and tolerances as in the first example. The only two changes compared to the previous example are:

- Using an increasing pressure,

$$p = k\bar{p}$$

  with $\bar{p} = 0.1$,

- computing a fixed number of 23 time steps with time step size $k = 1$.

The goals in this study are

- to observe the total length of the crack with respect to spatial mesh refinement; distribution of the COD.

The mesh and the initial crack are displayed in Figure 6. A sequence of crack patterns are provided in Figure 7. In fact, until time step 19, we only observe almost no growth. Then, since G_c is exceeded, we have brutal crack growth as also observed by [6] and [7] in the case of pure elasticity. A qualitative distribution of the COD is shown in Figure 8. Here, we notice that the COD has its largest value in the center of the crack and becomes smaller towards both tips. This is physically reasonable and a good criterion for validation. Finally, we compare the total crack length on three different meshes in Figure 9.

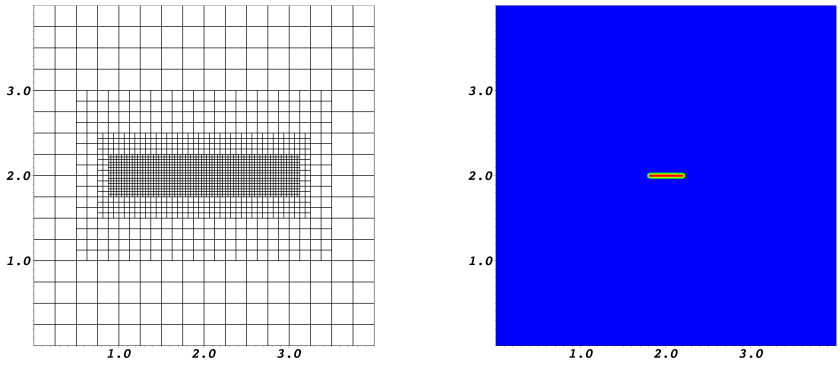

Figure 6: Example 2: Locally refined grid and initial crack pattern

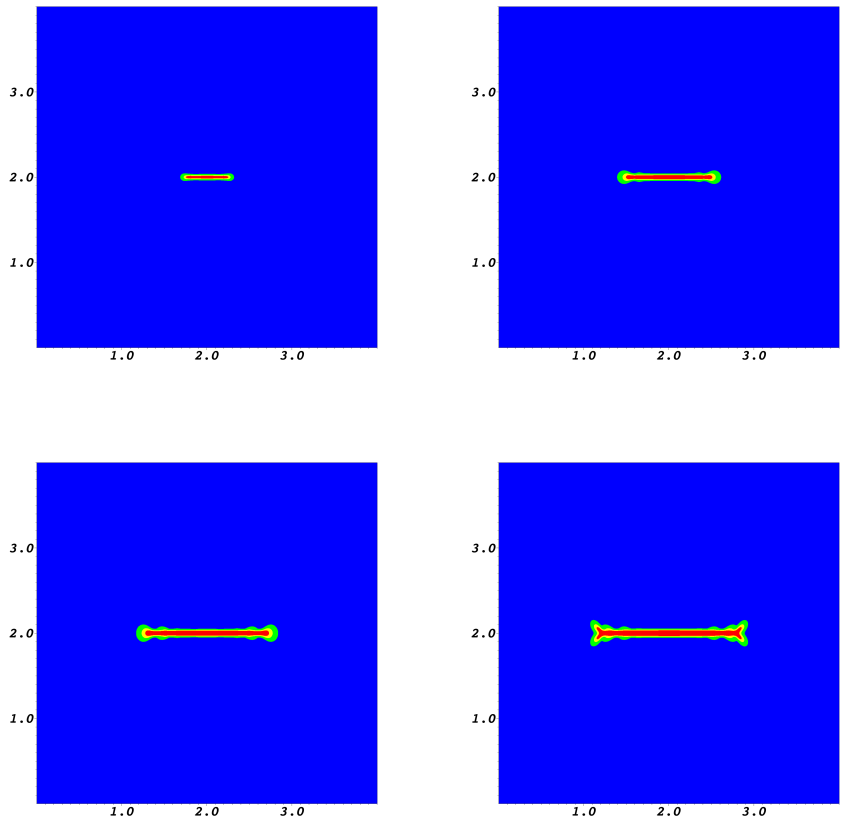

Figure 7: Example 2: Crack pattern for the last four time steps at $T = 20, 21, 22, 23$.

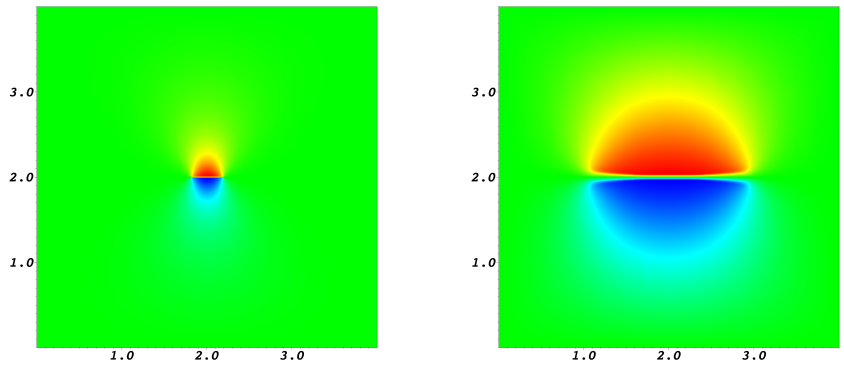

Figure 8: Example 2: Normal displacement (for the computation of the width) at the beginning and final times $T = 1, 23$. It is very important to notice that the color scheme and its density indicate that the COD has its largest value in the center of the crack and becomes smaller towards both tips. This is physically reasonable and a good criterion for validation.

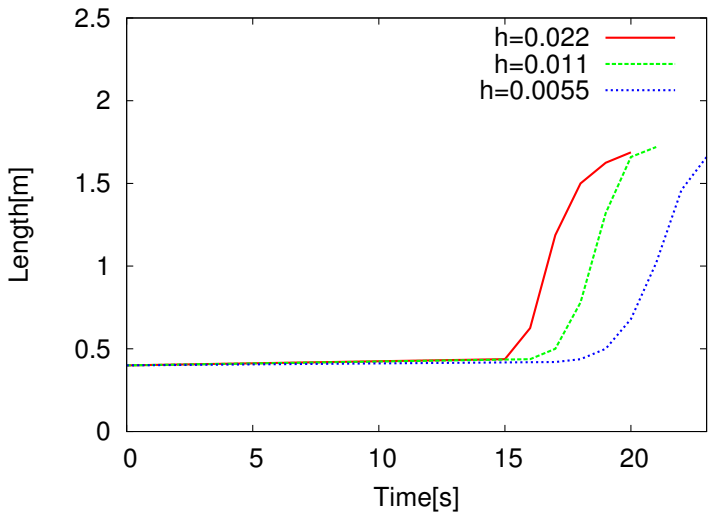

Figure 9: Example 2: Total crack length versus time on three mesh levels. In the plot, we have $h := h_{\min}$. The crack starts growing between time step 15 and 20 depending on the refinement level.

5.3. Increasing pressure leading to joining cracks

The third example demonstrates a major capability of the phase-field approach: joining of two cracks without using any special geometry-adapted technique. We keep all parameters as in the previous example. The first crack (named as crack 1) is the same as before and centered in the middle of the domain. The second crack (named as crack 2) is vertically-oriented at $x = 2.6$ and $1.8 \leq y \leq 2.2$ and is also extended by h in normal (here $x-$) direction. Consequently, the shortest distance of the two cracks is 0.4. As in the previous example, we compute 23 time steps with time step size $k = 1$. While applying an increasing pressure,

$$p = k\bar{p},$$

with $\bar{p} = 0.1$, we are able to study the propagation of both cracks and their joining. The goal is again to perform studies for different h and to detect the time when both cracks meet. Therefore, we observe the distance between the cracks. In addition, we perform a set of computations on a 10% distorted mesh. This is a good test, to see if the crack path is independent of the mesh structure (which of course should be the case!). The meshes are displayed in Figure 10.

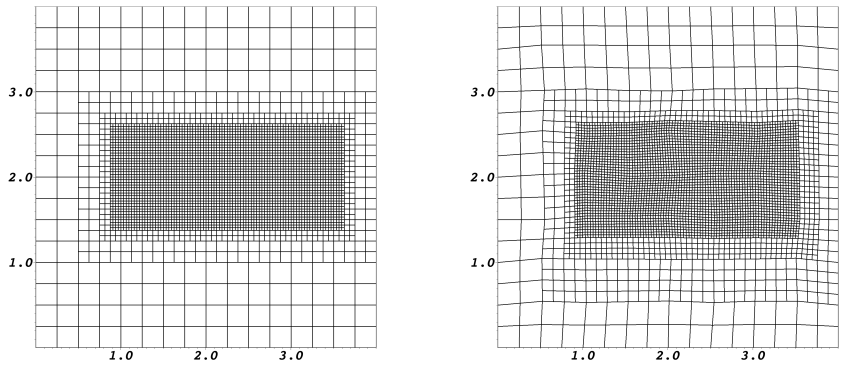

Figure 10: Example 3: Meshes for both sets of computations: locally refined mesh (left) and the same mesh but randomly distorted (right).

Observing the results provides us with the following understanding. In Figure 11, the four final crack patterns on the finest mesh are displayed. Before time step 20 almost no crack growth is observed. Then, brutal crack growth as in the previous example occurs. The final crack pattern to both meshes are shown in Figure 12. Indeed, the pattern is independent of the mesh-structure which is a very important observation. Quantitative findings to the brutal growth and the joining are provided for different meshes in Figure 13.

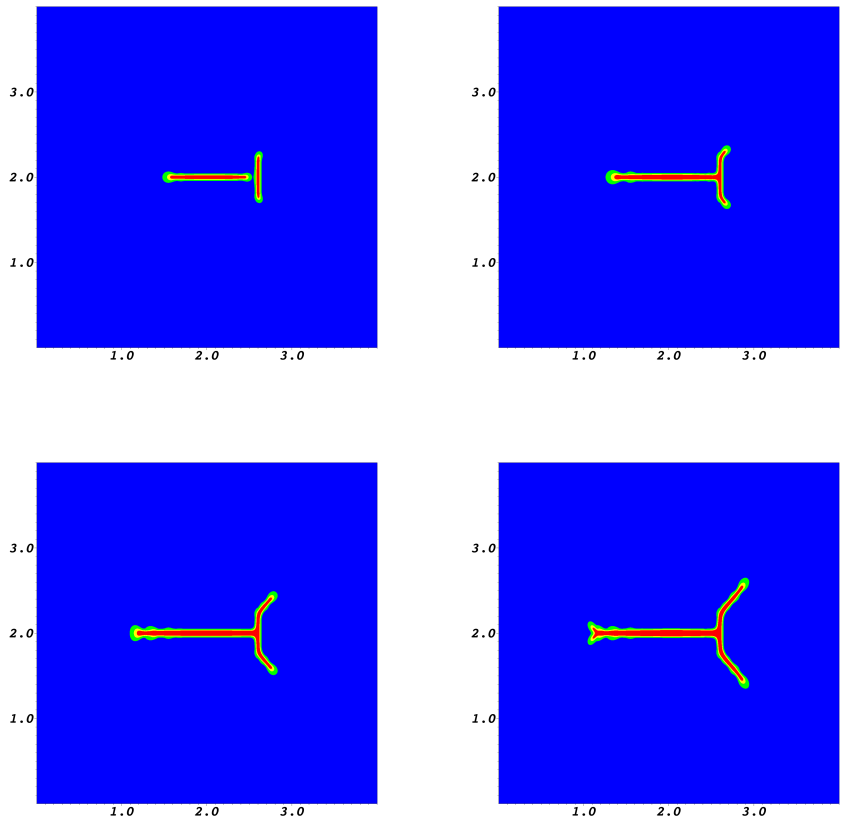

Figure 11: Example 3: Crack pattern for the last four time steps at $T = 20, 21, 22, 23$.

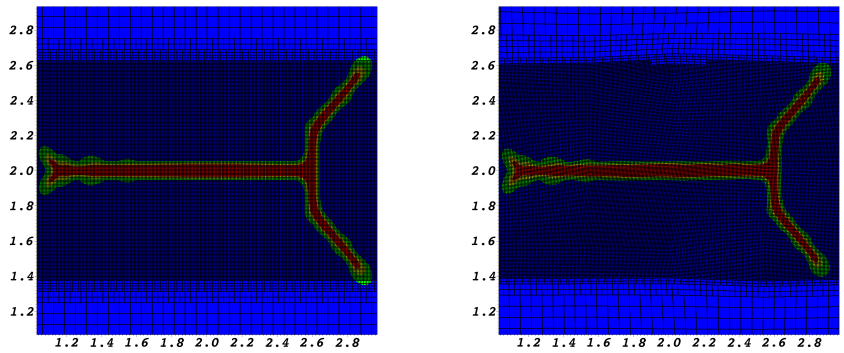

Figure 12: Example 3: Crack patterns for final time steps on the two different meshes with the distorted mesh on the right side. Comparing the graphical solutions, we observe that the crack pattern and propagation is independent of the mesh.

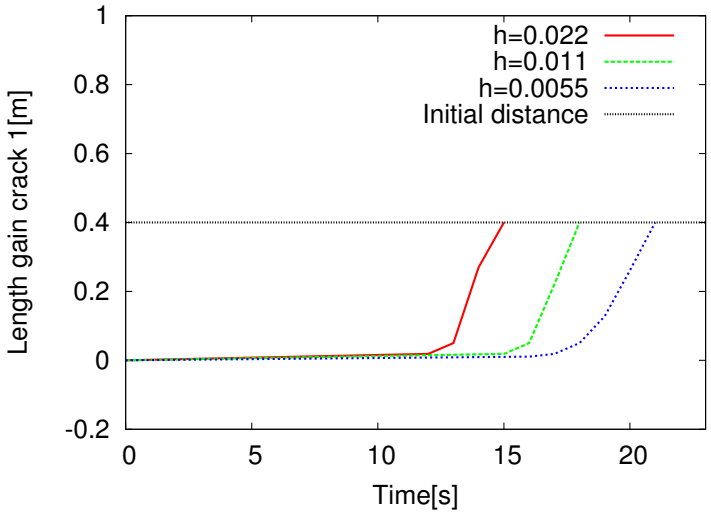

Figure 13: Example 3: Length gain of crack 1 into east direction. Both cracks join (at latest) when crack 1 reaches the center of crack 2. The initial distance between both cracks is 0.4.

5.4. Sneddon's 3d benchmark with constant pressure

In the final example, we upgrade our code to three dimensions. In the cube $\Omega = (0, 10)^3$, we prescribe a penny-shape crack with radius $r = 1.0$ in the $y = 5.0$-plane with mid-point $(5.0, 5.0, 5.0)$ and which is subject to a constant pressure $p_B = 10^{-3}$. The configuration and the initial crack are displayed in Figure 14 at top left. As boundary conditions we set the displacements zero on $\partial\Omega$. The material parameters (i.e., G_c, E, etc.) are the same as in the 2D examples. The initial penalization parameter is given by $\gamma = 10^2$. The tolerances are the same as in the 2D cases. The setup is again motivated by Sneddon and Lowengrub [27] (Chapter 3.3) who also provides an analytical expression to compute the normal displacements (from which we obtain the COD):

$$u_y = (r, y_m) = \frac{2(1-r)p_p}{\pi}\sqrt{1-(r-5)^2},$$

where $4 \leq r \leq 6$ (such that the radius of the penny-shape crack is ≤ 1) and $y_m = (5.0, 5.0, 5.0)$ denotes the origin of the penny-shape fracture. The results of the normal displacements are provided in Figure 15.

The goal of this test is twofold:

- Compare to Sneddon's analytical solution,
- Perform computations on different spatial mesh levels.

The evaluation of the COD is only performed with formula (18) because it has been shown in the 2D test that they deliver the same results.

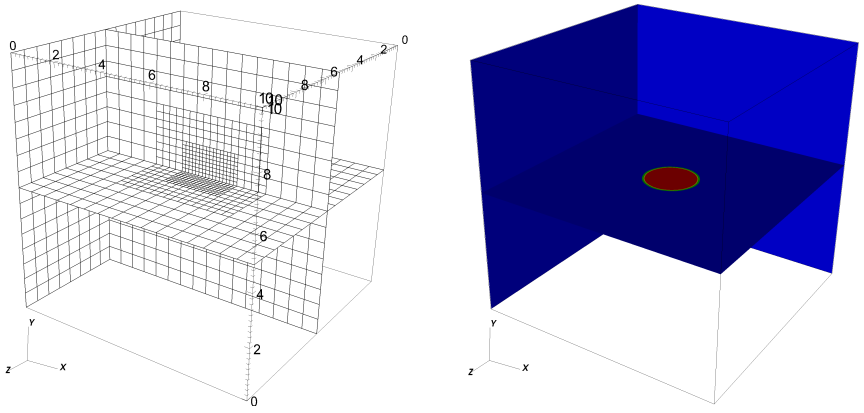

Figure 14: Example 4: Geometry information with locally refined grid and location of the penny-shape crack.

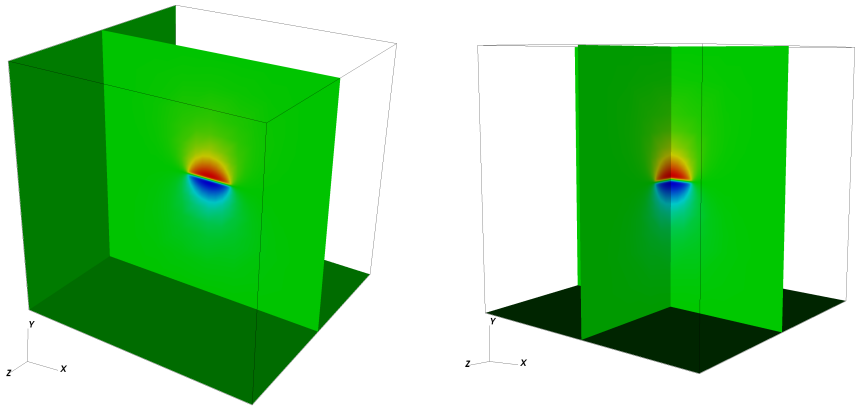

Figure 15: Example 4: Normal displacements for determining the COD.

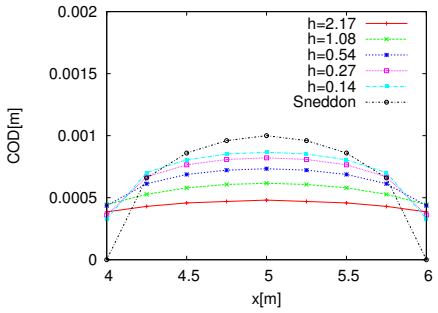

Figure 16: Example 4: COD for different h. Sneddon's black line line corresponds to his analytical 3D solution.

Analyzing our computations, we first notice that the time step tolerance is reached in 3 iterations (instead of 2 in the two-dimensional case). Our results show convergence with respect to spatial mesh refinement as illustrated in Figure 16. Moreover, the values converge towards the analytical solution. From both findings, we infer that our model works correctly. Finally, we aim to give a better understanding of our results and show several zoomed findings in Figure 17. In subfigure 1 (top left), we observe the location of the crack in the refined mesh. Of course, since we are only interested in the COD and no propagation, we adapted the local mesh refinement to the initial location of the crack. This could easily be adapted for propagating cracks as done in the 2D test cases or dynamically as described in the introduction to all four test cases. Specifically, we point out the volume approximation of the crack related to ε (and h) as shown in the subfigures 2 and 3. In subfigure 4, we emphasize that the largest crack opening is in the center of the crack and decreases towards the ends.

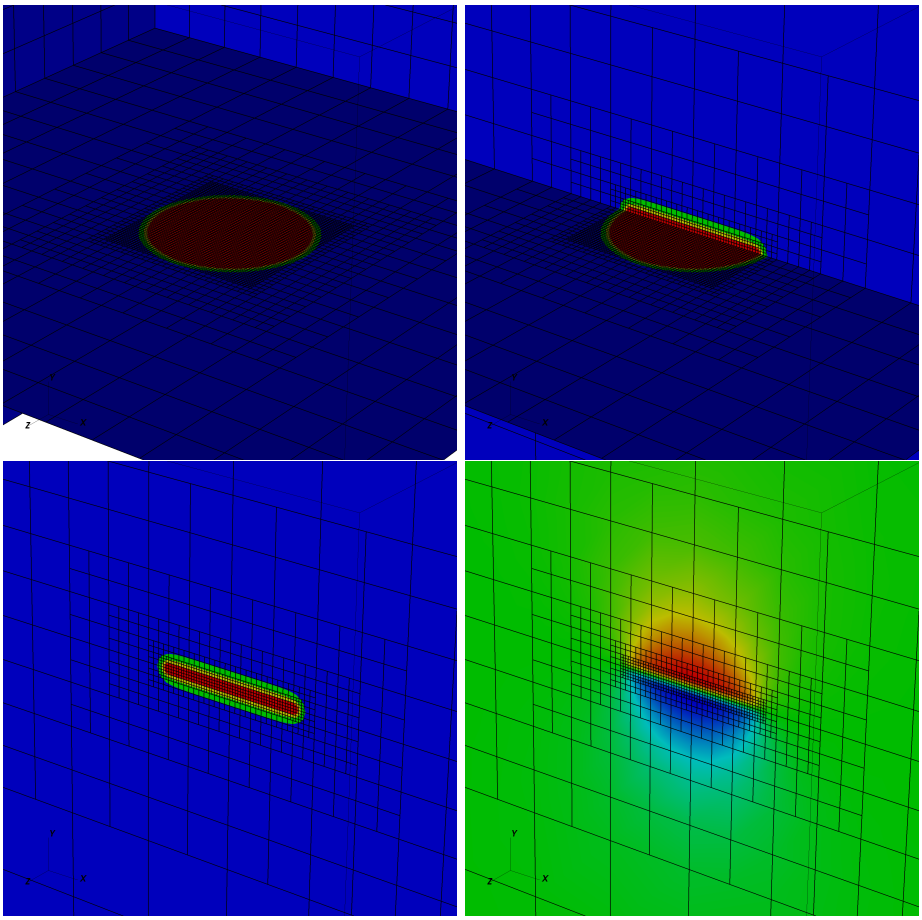

Figure 17: Example 4: Zoom-in in which the location (top left) and the volume approximation by extending in normal up- and down direction are illustrated (2nd and 3rd figure). Finally, a zoom-in to show the normal displacements is provided, which also shows that the largest crack opening is in the center of the crack and decreases towards the end (see also Figure 16).

6. Conclusions

In this work, we considered a phase-field formulation to solve pressurized fractures. In order to force the irreversibility of crack growth, a time inequality constraint is required, which is realized as a penalization. A robust method is based on the augmented Lagrangian approach which is substantiated with several numerical tests, namely pressurized propagating fractures, which are (still) very challenging to solve. Since detailed numerical studies are missing in the literature, we proposed simple, but challenging, configurations. As future extension, we plan to investigate three-dimensional propagating penny-shape fractures.

Acknowledgments

The third author thanks the Center for Subsurface Modeling at ICES, UT Austin, for hosting his research stay in July 2013 and the DAAD (German Academic Exchange Service) for a travel grant vital to the initialization of this collaboration. The second author is grateful to the Humboldt foundation, which supports from October 2013 other studies build upon the present work.

References

[1] A. Griffith, The phenomena of rupture and flow in solids., Philos. Trans. R. Soc. Lond. 221 (1921) 163–198.

[2] N. Moes, J. Dolbow, T. Belytschko, A finite element method for crack growth without remeshing, Int. J. Numer. Methods Engrg. 46 (1999) 131–150.

[3] I. Babuska, J. Belenk, The partition of unity method, Int. J. Numer. Methods Engrg. 40 (1997) 727–758.

[4] G. Francfort, J.-J. Marigo, Revisiting brittle fracture as an energy minimization problem, J. Mech. Phys. Solids 46 (1998) 1319–1342.

[5] B. Bourdin, G. Francfort, J.-J. Marigo, Numerical experiments in revisited brittle fracture, J. Mech. Phys. Solids 48 (2000) 797–826.

[6] B. Bourdin, G. Francfort, J.-J. Marigo, The variational approach to fracture, J. Elasticity 91 (2008) 1–148.

[7] C. Miehe, F. Welschinger, M. Hofacker, Thermodynamically consistent phase-field models of fracture: variational principles and multi-field fe implementations, International Journal of Numerical Methods in Engineering 83 (2013) 1273–1311.

[8] C. Miehe, M. Hofacker, F. Welschinger, A phase field model for rate-independent crack propagation: Robust algorithmic implementation based on operator splits, Comput. Meth. Appl. Mech. Engrg. 199 (2010) 2765–2778.

[9] M. J. Borden, C. V. Verhoosel, M. A. Scott, T. J. R. Hughes, C. M. Landis, A phase-field description of dynamic brittle fracture, Comput. Meth. Appl. Mech. Engrg. 217 (2012) 77–95.

[10] M. Hofacker, C. Miehe, Continuum phase field modeling of dynamic fracture: variational principles and staggered FE implementation, Int. J. Fract. 178 (2012) 113–129.

[11] A. Mikelić, M. Wheeler, T. Wick, A quasi-static phase-field approach to the fluid filled fracture, 2013. ICES Report 13-22, submitted for publication.

[12] B. Lecampion, E. Detournay, An implicit algorithm for the propagation of hydraulic fracture with a fluid lag, Comput. Meth. Appl. Mech. Engrg. 196 (2007) 4863–4880.

[13] B. A. Schrefler, S. Secchi, L. Simoni, On adaptive refinement techniques in multi-field problems including cohesive fracture, Comput. Meth. Appl. Mech. Engrg. 195 (2006) 444–461.

[14] B. Carrier, S. Granet, Numerical modeling of hydraulic fracture problem in permeable medium using cohesive zone model, Engineering fracture mechanics 79 (2012) 312–328.

[15] F. Irzal, J. J. Remmers, J. M. Huyghe, R. de Borst, A large deformation formulation for fluid flow in a progressively fracturing porous material, Comput. Meth. Appl. Mech. Engrg. 256 (2013) 29–37.

[16] B. Ganis, M. E. Mear, A. Sakhaee-Pour, M. F. Wheeler, T. Wick, Modeling hydraulic fractures with a reservoir simulator coupled to a boundary element method, Technical Report ICES Report 13-17, submitted, The University of Texas at Austin, 2013.

[17] S. Castonguay, M. Mear, R. Dean, J. Schmidt, Predictions of the growth of multiple interacting hydraulic fractures in three dimensions, SPE-166259-MS (2013) 1–12.

[18] B. Bourdin, C. Chukwudozie, K. Yoshioka, A variational approach to the numerical simulation of hydraulic fracturing, SPE Journal, Conference Paper 159154-MS, 2012.

[19] A. Mikelić, M. Wheeler, T. Wick, A phase-field approach to the fluid filled fracture surrounded by a poroelastic medium, 2013. ICES Report 13-15, submitted for publication.

[20] F. A. Lootsma, Hessian matrices of penalty functions for solving constrained-optimization problems, Philips Res. Repts. 24 (1969) 322–330.

[21] W. Murray, Analytical expressions for the eigenvalues and eigenvectors of the Hessian matrices of barrier and penalty functions, J. Optim. Theory Appl. 7 (1971) 189–196.

[22] M. R. Hestenes, Multiplier and gradient methods, J. Optimization Theory Appl. 4 (1969) 303–320.

[23] M. J. D. Powell, A method for nonlinear constraints in minimization problems, in: Optimization (Sympos., Univ. Keele, Keele, 1968), Academic Press, 1969, pp. 283–298.

[24] M. Fortin, R. Glowinski, Augmented Lagrangian Methods: Applications to the Numerical Solution of Boundary Value Problems, Stud. Math. Appl. 15, North Holland, Amsterdam, 1983.

[25] R. Glowinski, P. L. Tallec, Augmented Lagrangian and Operator-Splitting Methods in Nonlinear Mechanics, SIAM Stud. Appl. Math. 9, SIAM, Philadelphia, 1989.

[26] K. Ito, K. Kunisch, Lagrange Multiplier Approach to Variational Problems and Applications, volume 15 of *Advances in Design and Control*, Society for Industrial and Applied Mathematics (SIAM), Philadelphia, PA, 2008.

[27] I. N. Sneddon, M. Lowengrub, Crack problems in the classical theory of elasticity, SIAM series in Applied Mathematics, John Wiley and Sons, Philadelphia, 1969.

[28] T. Wick, Flapping and contact fsi computations with the fluid-solid interface-tracking/interface-capturing technique and mesh adaptivity, Comp. Mech. (2013).

[29] T. Wick, Solving monolithic fluid-structure interaction problems in arbitrary Lagrangian Eulerian coordinates with the deal.ii library, Archive of Numerical Software 1 (2013) 1–19.

[30] W. Bangerth, T. Heister, G. Kanschat, et al., Differential Equations Analysis Library, 2012.

[31] I. N. Sneddon, The distribution of stress in the neighbourhood of a crack in an elastic solid, Proc. R Soc London A 187 (1946) 229–260.